J. Non-Newtonian Fluid Mech. 165 (2010) 1204–1218

Contents lists available at ScienceDirect

Journal of Non-Newtonian Fluid Mechanics

journal homepage: www.elsevier.com/locate/jnnfm

Viscoelastic flow in a two-dimensional collapsible channel

Debadi Chakraborty[a], Mohit Bajaj[b,1], Leslie Yeo[b], James Friend[b], Matteo Pasquali[c], J. Ravi Prakash[a,*]

[a] Department of Chemical Engineering, Monash University, Melbourne, VIC 3800, Australia
[b] Department of Mechanical Engineering, Monash University, Melbourne, VIC 3800, Australia
[c] Department of Chemical and Biomolecular Engineering, MS 362, Rice University, Houston, TX 77005, USA

ARTICLE INFO

Article history:
Received 28 November 2009
Received in revised form 6 June 2010
Accepted 9 June 2010

Keywords:
Two-dimensional collapsible channel flow
Viscoelastic fluid flow
Fluid–structure interactions
Blood flow
Conformation tensor models
Finite element method

ABSTRACT

We compute the flow of three viscoelastic fluids (Oldroyd-B, FENE-P, and Owens blood model) in a two-dimensional channel partly bounded by a tensioned membrane, a benchmark geometry for fluid–structure interactions. The predicted flow patterns are compared to those of a Newtonian liquid. We find that computations fail beyond a limiting Weissenberg number. Flow fields and membrane shape differ significantly because of the different degree of shear thinning and molecular extensibility underlying the three different microstructural models.

1. Introduction

Blood is a concentrated suspension of multiple components with a complex rheological behaviour; it interacts intricately with blood vessel walls—both chemically and mechanically. A quantitative description of physiological blood circulation requires understanding blood rheology as well as the effect of the architectural and mechanical properties of the vascular system. *Microcirculation* refers to blood flow in small vessels (arterioles, venules, and capillaries), whereas macrocirculation encompasses flow in larger arteries. From a fluid mechanical viewpoint, the microcirculation corresponds to flows at low Reynolds number *Re*, while the macrocirculation corresponds to flows where inertia is significant. Despite the commonalities (e.g., interaction between blood and vessel walls) the micro and macrocirculation are sufficiently different to warrant different modelling approaches. In the high *Re* flows in medium and large arteries (macrocirculation), inertial forces dominate and tube diameters are large; therefore, the Navier–Stokes equations provide an adequate model [1]. Most studies on fluid–structure interaction in blood flow have focused on the macrocirculation. Conversely, inertia plays little role in the microcirculation; here, the non-Newtonian behaviour of blood (due to its particulate microstructure) must be captured—specifically, shear thinning at low shear rates, and its viscoelastic and thixotropic nature [1–3]. So far, there have been no studies of fluid–structure interaction issues associated with the flow of viscoelastic fluids in vessels with compliant walls. This work aims to study the flow of model viscoelastic fluids in a simple two-dimensional collapsible channel as a preliminary study of the behaviour that might arise when more realistic models of blood and blood vessels are simulated under conditions in which the viscoelastic character of blood and the elastic nature of blood vessel walls become important.

Laboratory experiments on flow through collapsible tubes have shown complex and non-linear dynamics, with a multiplicity of self-excited oscillations [4,5]. The simplest literature numerical model that captures part of this rich behaviour is that of a fluid flowing in a 2D rigid parallel sided channel, where part of one wall is replaced by a tensioned membrane (Fig. 1). This geometry has been studied extensively in the case of Newtonian fluids, with the flexible wall treated as an elastic membrane of zero thickness, with the stretching and the bending stiffness of the membrane along the flow direction neglected [6–10]. More recently, this basic model has been improved by including more realistic treatments of the elastic wall and extending the geometry to handle 3D compliant tubes [11–16]. All these studies treated the fluid as Newtonian. Here, we use the simple 2D geometry, with a zero-thickness membrane, to study fluid–structure interaction in viscoelastic liquids, restricted to $Re = 1$.

The shear thinning of blood [1–3] is due to the spontaneous arrangement of red blood cells into rouleaux, aggregates

* Corresponding author. Tel.: +61 3 9905 3274; fax: +61 3 9905 5686.
E-mail address: ravi.jagadeeshan@eng.monash.edu.au (J.R. Prakash).
[1] Present address: IBM India Pty Ltd., Bangalore 560045, India.

0377-0257/$ – see front matter © 2010 Elsevier B.V. All rights reserved.
doi:10.1016/j.jnnfm.2010.06.005

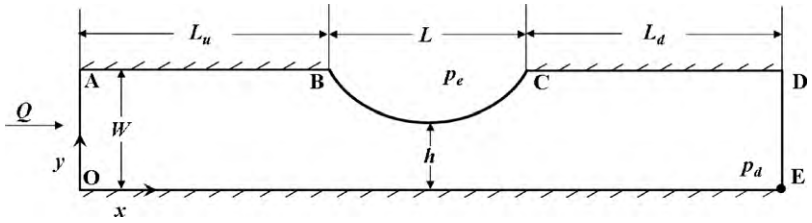

Fig. 1. Geometry of the 2D collapsible channel; the segment BC is an elastic membrane. Here, Q is the flow rate, p_e is the external pressure on the membrane, p_d is the pressure on the wall at the downstream boundary (denoted by location E), W is the width of the channel, L the length of the deformable membrane, and h is the minimum height of the gap between the bottom wall of the channel and the deformable membrane.

resembling stacks of coins. These aggregates form three-dimensional structures in the absence of flow. At low shear rates, the viscosity is high and is controlled by the size and interaction of the rouleaux. At high shear rates, the rouleaux break, leading to lower viscosity. Numerous models have been proposed for the rheological behaviour of blood [17–24]. Models that account for blood viscoelasticity are commonly generalised Maxwell models, with a relaxation time and shear viscosity that depends on a dynamical structural variable describing the aggregation/disaggregation of red blood cells. The recent models by Owens and co-workers [23,24] are appealing because the evolution equation for the structural variable is derived through a microstructural framework based on transient polymer network theory. Predictions of these models compare very well with a range of experimental data on blood rheology [23,25,26]. Owens original model [23] addresses flows where the concentration of blood cells is uniform; it was extended recently [24] to include flow-induced concentration gradients, which are known to develop, for example, when the length scale of the flow approaches that of the blood cells—the Fåhraeus [27] and Fåhraeus–Lindqvist [28] effects. Here we use the original Owens models [23] (slightly modified to handle non-homogeneous flows, and restricted to the single-mode version) to study the flow of blood in a compliant channel, and compare the results to those obtained with two "standard" viscoelastic fluid models—Oldroyd-B and FENE-P.

The flow and membrane shape are computed simultaneously with the DEVSS-TG/SUPG (discrete elastic viscous stress split-traceless gradient) finite element method extended to free boundary problems [29]. The constitutive equations of all models are written in conformation tensor form [30].

This article is organized as follows. Section 2 presents the problem formulation and viscoelastic models. Section 3 compares the results of viscoelastic and Newtonian fluid computations, and Section 4 summarises our conclusions.

2. Problem formulation

The geometry of the flow is that of a 2D channel, with one of the walls containing an elastic segment. The membrane has zero thickness. In units of channel width W, the dimensions of the channel are $L_u = 7W$, $L = 5W$, and $L_d = 7W$ (Fig. 1). As in Luo and Pedley [8], the tension in the flexible wall is constant and the shape of the flexible part is governed by the normal force acting on it. h denotes the *minimum* channel width between the deformed membrane and the bottom wall (Fig. 1).

2.1. Governing equations

The equations of motion for steady, incompressible flow in the absence of body forces are:

$$\nabla \cdot \mathbf{v} = 0 \tag{1}$$

$$\rho \mathbf{v} \cdot \nabla \mathbf{v} = \nabla \cdot \mathbf{T} \tag{2}$$

where ρ is the density of the liquid, $\mathbf{v}$ is the velocity, ∇ denotes the gradient. The Cauchy stress tensor is $\mathbf{T} = -p\mathbf{I} + \boldsymbol{\tau} + \boldsymbol{\sigma}$, where p is the pressure, $\mathbf{I}$ is the identity tensor, $\boldsymbol{\tau}$ is the viscous stress tensor and $\boldsymbol{\sigma}$ is the elastic stress tensor. The viscous stress tensor is $\boldsymbol{\tau} = 2\eta_s \mathbf{D}$, where η_s is the solvent viscosity and $\mathbf{D} = \frac{1}{2}(\nabla \mathbf{v} + \nabla \mathbf{v}^T)$ is the rate of strain tensor.

The elastic stress depends on the microstructural state of the fluid, represented here by the dimensionless conformation tensor $\mathbf{M}$ [30]. For the Oldroyd-B and FENE-P models, this relation is well known; it takes the form,

$$\boldsymbol{\sigma} = \frac{\eta_{p,0}}{\lambda_0}\{f(\mathrm{tr}\,\mathbf{M})\mathbf{M} - \mathbf{I}\} \tag{3}$$

where $\eta_{p,0}$ is the contribution of the microstructural elements to the zero shear rate viscosity, and λ_0 is the constant characteristic relaxation time of the microstructure. For the Oldroyd-B model, $f(\mathrm{tr}\,\mathbf{M}) = 1$, while for the FENE-P model [30],

$$f(\mathrm{tr}\,\mathbf{M}) = \frac{b_{\mathbf{M}} - 1}{b_{\mathbf{M}} - \mathrm{tr}\,\mathbf{M}/3} \tag{4}$$

where $b_{\mathbf{M}}$ is the finite extensibility parameter, defined as the ratio of maximum length squared of the microstructural element to its average length squared at equilibrium. The conformation tensor obeys the following evolution equation,

$$\frac{\partial \mathbf{M}}{\partial t} + \mathbf{v} \cdot \nabla \mathbf{M} - \nabla \mathbf{v}^T \cdot \mathbf{M} - \mathbf{M} \cdot \nabla \mathbf{v} = -\frac{1}{\lambda_0}\{f(\mathrm{tr}\,\mathbf{M})\mathbf{M} - \mathbf{I}\} \tag{5}$$

The Owens blood model [23] was originally presented in terms of a constitutive equation for the elastic stress and has not yet been translated into conformation tensor form and studied in complex flows. A conformation tensor version of the Owens model can be derived straightforwardly, noting that Eqs. (3) and (5) hold for the Owens model (with $f(\mathrm{tr}\,\mathbf{M}) = 1$, as in the Oldroyd-B model). However, while Eq. (3) remains unchanged with λ_0 denoting the *zero shear rate* relaxation time, it is replaced in Eq. (5) by a function λ, which represents the relaxation time of the elastic stress due to blood cell aggregates. λ depends on the average size of the blood cell aggregates, n, which is controlled by the competition of spontaneous aggregation and flow-induced disaggregation. We assume here that the dynamics of n are fast with respect to other changes of the flow, i.e., $n = n_{st}(\dot{\gamma})$—its equilibrium value based on the local shear rate $\dot{\gamma} = \sqrt{2\,\mathbf{D} : \mathbf{D}}$. This choice preserves the viscoelastic and shear thinning character of blood but does not capture its thixotropic behaviour [23]. This simplification makes it unnecessary to solve an additional equation for the variation of n in the flow domain. Under this assumption, the relaxation time λ is

$$\lambda = \left(\frac{\lambda_H}{\eta_{p,\infty}}\right)\eta_p(\dot{\gamma}) \tag{6}$$

where λ_H is the relaxation time of individual blood cell aggregates, $\eta_{p,\infty}$ is the infinite shear-rate viscosity, and $\eta_p(\dot{\gamma})$ is their contribu-

tion to blood viscosity given by the Cross model,

$$\eta_p(\dot{\gamma}) = \eta_{p,0}\left(\frac{1+\theta_1\dot{\gamma}^m}{1+\theta_2\dot{\gamma}^m}\right) \tag{7}$$

where m is a power-law index, and the ratio of parameters θ_1 and θ_2 satisfies the expression, $\theta_1/\theta_2 = \eta_{p,\infty}/\eta_{p,0}$ [23]. The values of all model parameters are reported in Section 2.3.

To handle free boundaries, we use a boundary fitted finite element based elliptic mesh generation method [29,31–33] which involves solving the following elliptic differential equation for the mapping $\mathbf{x} = \mathbf{x}(\boldsymbol{\xi})$,

$$\nabla \cdot \tilde{\mathbf{D}} \cdot \nabla \boldsymbol{\xi} = \mathbf{0} \tag{8}$$

where $\boldsymbol{\xi}$ is a vector of positions in the computational domain and the dyadic, $\tilde{\mathbf{D}}$, is a function of $\boldsymbol{\xi}$, analogous to a diffusion coefficient, which controls the spacing of the coordinate lines [33].

2.2. Boundary conditions and discretisation

We prescribe the following boundary conditions:

1. At the upstream boundary, a fully developed velocity profile is specified in the form, $v_x = f(y)$, and $v_y = 0$. Since, for all the *Wi* considered here, the upstream velocity profiles for the Oldroyd-B and FENE-P fluids do not differ significantly from that for a Newtonian fluid, a Newtonian velocity profile is used. However, for the Owens model fluid, we use a fully developed velocity profile obtained by analytically solving the flow of a power-law fluid in a channel. This is because of the strongly shear thinning nature of the Owens model fluid. The power-law index used is that exhibited by the Owens model (with the current parameter values) in a simple shear flow.
2. No slip boundary conditions ($\mathbf{v} = \mathbf{0}$) are applied on the rigid walls.
3. At the flexible wall,
   (a) On the *momentum* equation, we impose (i) $\mathbf{t} \cdot \mathbf{v} = 0$, where $\mathbf{t}$ is the unit tangent to the flexible wall, and, (ii) a force balance in the normal direction through the traction boundary condition:

   $$\mathbf{nn} : \mathbf{T} = -p_e + \chi \nabla_{II} \cdot \mathbf{n} \tag{9}$$

   where $\mathbf{n}$ is the unit normal to the flexible wall, ∇_{II} denotes the surface gradient operator, p_e is the external pressure and χ is the fixed tension in the flexible wall.
   (b) On the *mapping* equation, we impose (i) $\mathbf{n} \cdot \mathbf{v} = 0$ in the normal direction, and, (ii) a uniform node distribution in the tangential direction.
4. At the downstream boundary, the fully developed flow boundary condition is imposed, $\mathbf{n} \cdot \nabla \mathbf{v} = \mathbf{0}$.
5. At the upstream inflow, the conformation tensor does not change along the streamlines because the flow is fully developed [29,34]. Thus,

   $$\mathbf{v} \cdot \nabla \mathbf{M} = \mathbf{0} \tag{10}$$

6. The pressure of the fluid at the downstream boundary, p_d, is set equal to zero on the bottom wall (at location E in Fig. 1).

Eqs. (1)–(8) are converted into a set of algebraic equations by the DEVSS-TG finite element method [29,35], which introduces the traceless interpolated velocity gradient $\mathbf{L}$ [29]

$$\mathbf{L} - \nabla \mathbf{v} + \frac{1}{\mathrm{tr}\mathbf{I}}(\nabla \cdot \mathbf{v})\mathbf{I} = \mathbf{0} \tag{11}$$

In the transport equations the rate of strain tensor $\mathbf{D}$ is calculated from the interpolated velocity gradient $\mathbf{L}$.

The weighted residual form of Eqs. (1), (2), (5), (8) and (11), yields a large set of coupled non-linear algebraic equations, solved by Newton's method with analytical Jacobian, frontal solver, and first order arc length continuation in parameters [29,36,37].

2.3. Dimensionless numbers and choice of parameter values

Non-dimensionalization of the governing equations and boundary conditions yields the following dimensionless numbers:

$$Re = \frac{\rho W U_0}{\eta_0}; \quad \beta = \frac{\eta_s}{\eta_0}; \quad Wi = \frac{\lambda_0 U_0}{W}; \quad Ca = \frac{\eta_0 U_0}{\chi};$$
$$P_d = \frac{(p_e - p_d)W}{\eta_0 U_0} \tag{12}$$

where U_0 is the average inlet velocity, *Ca* is analogous to a capillary number, β is the viscosity ratio, *Wi* is the *inlet* Weissenberg number, P_d is the dimensionless transmural pressure difference, and $\eta_0 = \eta_s + \eta_{p,0}$ is the zero shear rate solution viscosity. (For a Newtonian fluid, η_0 is just the constant Newtonian viscosity). It is convenient to define a *local* Weissenberg number $\widetilde{Wi} = \lambda_0 \dot{\gamma}$, which measures the non-dimensional shear rate anywhere in the flow.

Luo and Pedley [8] used the dimensionless ratio, $\alpha = Ca/Ca^*$ to represent the influence of membrane tension, where Ca^* is a reference dimensionless tension (defined with $\chi = 1.610245$ N/m). In order to compare our predictions for Newtonian fluids at $Re = 1$ to Ref [8], we also index membrane tension by α (in the range α =15–64), and we use the same value of the dimensionless transmural pressure difference, $P_d = 9.3 \times 10^4$.

For the Owens model, the best agreement with triangular step shear-rate experimental data [38] occurs when parameters $\eta_{p,0} = 0.14$ Pa s, $\eta_{p,\infty} = 0.004$ Pa s, $\theta_2 = 7.2$, $m = 0.6$, and $\lambda_H = 0.145$ s [23]. Interestingly, this choice of parameters neglects the solvent (or plasma) viscosity, and consequently yields an upper convected Maxwell" rather than an "Oldroyd-B" type model. Later work [25,24] introduced a solvent contribution ($\eta_s = 0.001$ Pa s), and modified the remaining parameters depending on the specific comparison of model predictions with experiments. Importantly, in steady homogeneous flows, specification of the parameters above also sets the expression of the relaxation time $\lambda(\dot{\gamma})$. Here we vary λ_H to control the inlet Weissenberg number (since $\lambda_0 = (\eta_{p,0}/\eta_{p,\infty})\lambda_H$), while keeping the values of the other parameters [23], augmented with the plasma viscosity $\eta_s = 0.001$ Pa s.

To attain $Re = 1$, we set $\rho = 1054$ kg/m^3 (as in Ref. [23]), $U_0 = 1.338 \times 10^{-2}$ m/s, $W = 10^{-2}$ m and $\eta_0 = 0.141$ Pa s. This yields a viscosity ratio $\beta = 0.0071$ (which signifies that the fluid is predominantly elastic). The FENE-P parameter $b_{\mathbf{M}}$ is set to 100.

3. Results and discussions

3.1. Code validation

We compare of our prediction of membrane shape for a Newtonian fluid to those of Luo and Pedley [8] (a similar comparison was reported earlier in Ref. [12]). The difference between external p_e and outlet p_d pressures is one of the parameters that determines the velocity and stress fields in the channel [8,9]. In Newtonian flow, our downstream boundary condition is equivalent to that used by Luo and Pedley [8]; to allow direct comparison, we use their same downstream channel length.

Fig. 2 shows the profile of the membrane at different values of α. Our results are in excellent agreement with Ref. [8]. Notably, Luo and Pedley [8] reported that steady states could be computed directly only at high membrane tension—i.e., low $\alpha < 64$ at $Re = 1$ [8]—whereas time dependent simulations were necessary to compute steady solutions at higher α (for sufficiently small *Re*) [9].

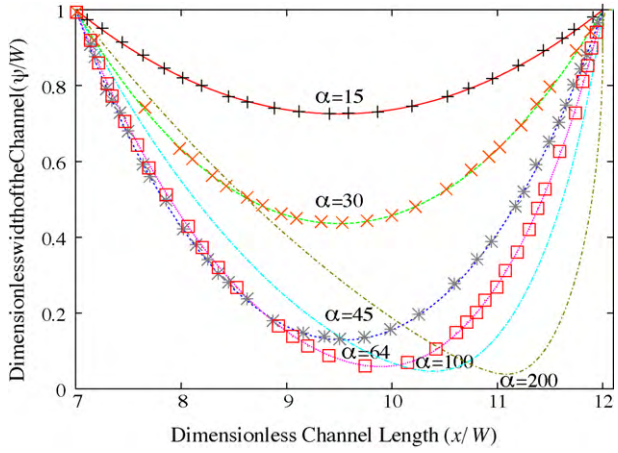

Fig. 2. The deformed shape of the flexible wall for the steady flow of a Newtonian fluid in the 2D collapsible channel, at various values of the dimensionless membrane tension ratio α. Lines denote the result of the current FEM simulation, while the symbols are the reported results of Luo and Pedley [8].

Our fully coupled algorithm shows no such convergence limits at $Re = 1$; profiles for $\alpha = 100$ and 200 are displayed in Fig. 2. This demonstrates the robustness of the present simulation technique.

3.2. Mesh convergence and the limiting Weissenberg number

Viscoelastic flows are notoriously difficult to compute; therefore, here we study mesh convergence over a range of parameters, particularly to establish whether the collapsible channel flow suffers from the high Weissenberg number problem.

Computations are performed with three different meshes (M1, M2 and M3) (Fig. 3 and Table 1).

The invariants of the conformation dyadic, **M** are a good indicator of mesh convergence; its eigenvalues m_i represent the square stretch ratios along the principal directions of stretching $\boldsymbol{m_i}$ for an ensemble of molecules [29,30]. Previous studies have shown that the breakdown of viscoelastic computations coincides with the smallest eigenvalue becoming negative in some regions of the flow domain [29,37,39,40].

Figs. 4 and 5 show the contour plots of the largest (m_3) and smallest (m_1) eigenvalues for the Oldroyd-B, FENE-P and Owens models, at $Wi = 0.1$ and $\alpha = 30$. They indicate that the molecules experience varying extents of stretching and contraction as they flow in the channel and below the collapsible wall. For all the models, the largest eigenvalue is highest below the collapsible wall at the minimum gap location (Fig. 4). (The magnitude varies from model to model.) The smallest eigenvalue is positive everywhere in the flow domain (Fig. 5, $Wi = 0.1$).

Raising Wi yields higher maximum m_3 and lower minimum m_1 across the flow domain, as shown in Fig. 6 for the Owens model at $\alpha = 30$ and $\alpha = 45$. Whereas the maximum m_3 grows smoothly with Wi and results on various meshes overlap (Fig. 6(b) and (d)), the plots of minimum m_1 show clearly the breakdown of each mesh (Fig. 6(a) and (c)). Even though we have not carried out computations with a mesh finer than M3, the sudden change of slope of the curves in Fig. 6(c) suggests that M3 mesh is yielding inaccurate

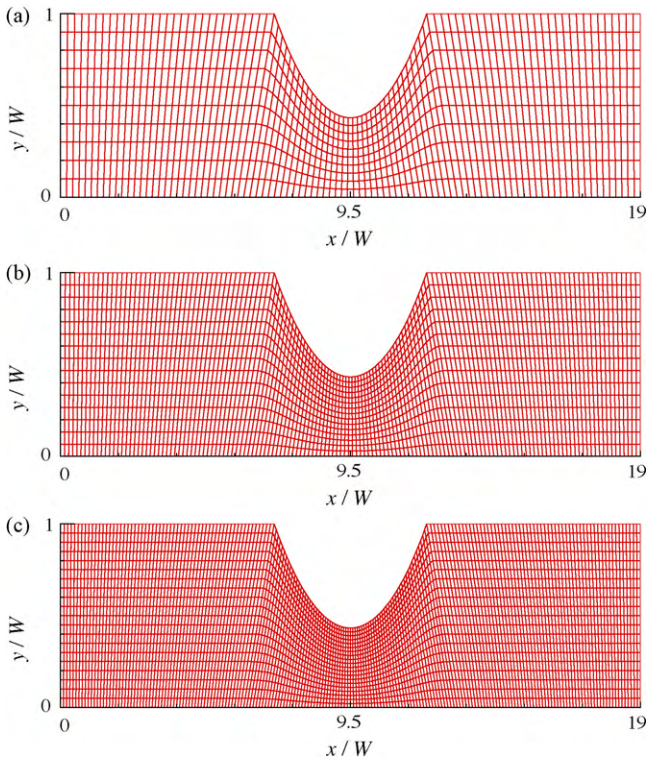

Fig. 3. Meshes M1 (a), M2 (b) and M3 (c), considered in the current study.

results at $Wi \gtrsim 0.5$ at $\alpha = 45$. Unless otherwise specifically stated, all computations reported hereafter were performed on M3.

On any mesh, computations can be performed at Wi beyond the limit of mesh convergence, until a limiting Weissenberg number, beyond which computations fail because the minimum value of m_1 becomes negative (which is unphysical)—this is clearly visible in Fig. 6(a) and (c). As has been observed in previous studies [29,37], the maximum attainable value of Wi increases with mesh refinement; for example, in the Owens model at $\alpha = 45$, the limiting value of the Weissenberg number is $Wi = 0.75$ on M2 and $Wi = 0.9$ on M3. Fig. 6(a) and(c) shows that the tension ratio affects the limiting Weissenberg number (because it affects the minimum gap); For the Owens model, the limiting Weissenberg number (on M3) decreases from $Wi = 7.0$ at $\alpha = 30$ to $Wi = 0.9$ at $\alpha = 45$.

The decrease of the minimum eigenvalue below zero coincides with a steep increase in the maximum eigenvalue (Fig. 6(b) and (d)). This value is much higher for $\alpha = 45$ than for $\alpha = 30$ because (as in the Newtonian case, Fig. 2) the minimum gap h decreases with increasing α, leading to a more dramatic "squeezing" of the fluid, and a consequently greater stretching of the molecules in the gap.

Computations with the Oldroyd-B and FENE-P models yield qualitatively similar behaviour; the limiting Wi values are reported in Table 2 for $\alpha = 30$ and $\alpha = 45$.

Fig. 7 shows the dependence of the limiting Weissenberg number on the tension ratio for the three different fluid models. In general, the limiting Weissenberg numbers follow the trend

Table 1
Meshes considered in the current study.

Mesh	Number of elements	Number of nodes	Degrees of freedom for fully coupled macroscopic simulations (**x**, **v**, p, **M**, **L**)
M1	950	4011	27,342
M2	2145	8897	60,455
M3	3800	15,621	105,972

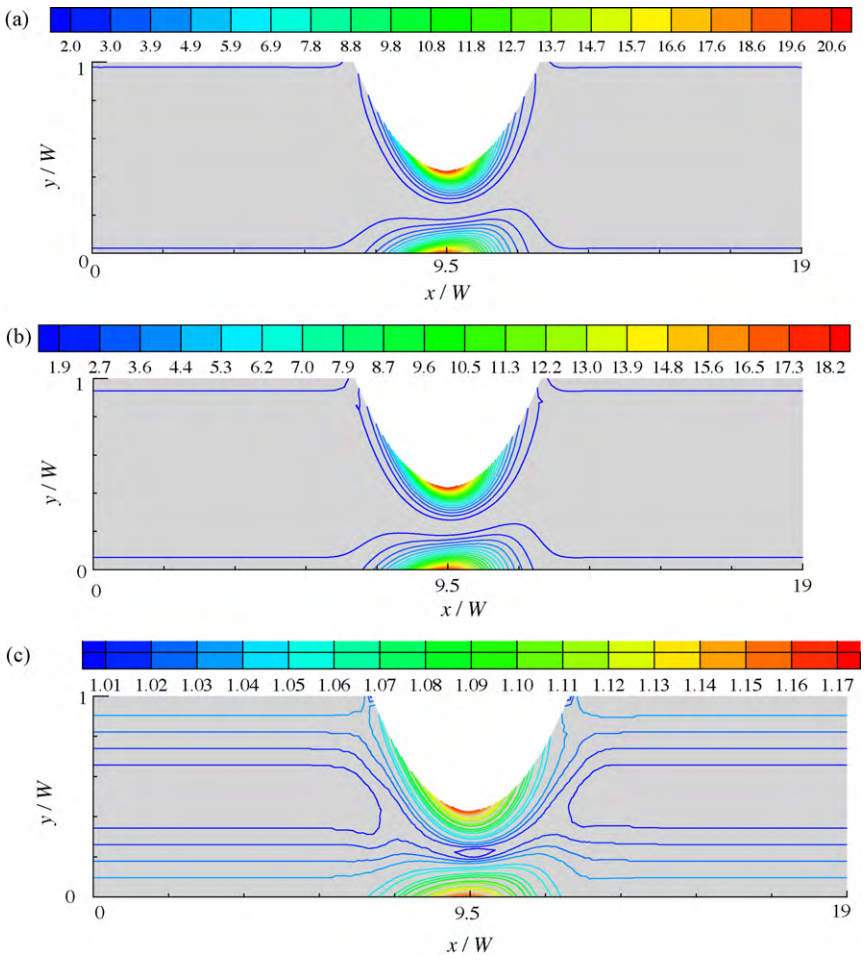

Fig. 4. Contour plots of the largest eigenvalues (m_3) of the conformation tensor at $Wi = 0.1$ for: (a) Oldroyd-B, (b) FENE-P, and (c) Owens models, at a tension ratio $\alpha = 30$.

Owens > FENE-P > Oldroyd-B until a tension ratio $\alpha \approx 50$, where there is an interesting crossover, and the limiting Weissenberg number for the Owens model becomes smaller than that for the FENE-P model.

Fig. 8 shows the profile of M_{xx} (mean streamwise molecular stretch) across the minimum gap at $\alpha = 45$ for a range of Weissenberg numbers and all three fluid models. Clearly, with increasing Wi, M_{xx} grows almost symmetrically, from a relatively low value in the middle of the gap, to a significantly larger value near the bottom (rigid) and top (flexible) walls. In the Oldroyd-B and Owens models, M_{xx} is unbounded. Conversely, the FENE-P model has an upper bound for the maximum M_{xx}, which for $b_{\mathbf{M}} = 100$ is 300. This upper bound for the FENE-P model limits the M_{xx} cross-stream gradient near the walls; such saturation is not present in the M_{xx} profiles for the Oldroyd-B and Owens models, which display steep gradients near the walls. Interestingly, of the three fluid models, the FENE-P model shows the highest stretch in the center of the gap.

Table 2
Maximum mesh converged value of Wi, and the limiting Wi for the three fluid models, for computations carried out with the M2 and M3 meshes, at two values of α.

	$\alpha = 30$				$\alpha = 45$			
	Converged Wi		Limiting Wi		Converged Wi		Limiting Wi	
	M2	M3	M2	M3	M2	M3	M2	M3
Oldroyd-B	0.2	0.43	0.42	0.44	0.02	0.04	0.06	0.07
FENE-P	0.32	0.45	0.50	0.53	0.2	0.27	0.25	0.27
Owens	4.0	5.0	6.45	6.76	0.3	0.5	0.75	0.9

Before examining the effect of fluid behaviour on flow characteristics, it is important to note that both the Oldroyd-B and Owens models predict an unbounded conformation tensor and extensional viscosity in a steady, homogeneous extensional flow, whereas the FENE-P model has a bound on these quantities. Moreover, the Oldroyd-B model predicts constant viscosity in steady shear flow, whereas the FENE-P and Owens models are shear thinning.

3.3. Velocity fields and molecular shear and extension rates

Fig. 9 compares the velocity contours predicted for a Newtonian fluid with the contours predicted for the Oldroyd-B, FENE-P and Owens model fluids at $Wi = 0.01$ and $\alpha = 45$. While the fields for the Newtonian, Oldroyd-B and FENE-P fluids do not differ to any significant degree from each other at this value of Wi (Fig. 9(a)), the velocity profile for the Owens model displays a slight difference from the Newtonian profile (Fig. 9(b)). Interestingly, this apparently slight difference in the velocity field between the different models becomes greatly amplified when viewed from the perspective of *molecular* deformation rates, as elaborated below.

Arguing that the invariants of the rate of strain cannot serve as indicators of the type of flow because they do not carry any information on whether molecules are being strained persistently along the same axes, or are rotating with respect to the principal axes of the rate of strain, Pasquali and Scriven [30] introduced the molecular extension and shear rates as being more appropriate measures for obtaining insight into the coupling between the flow and molecular

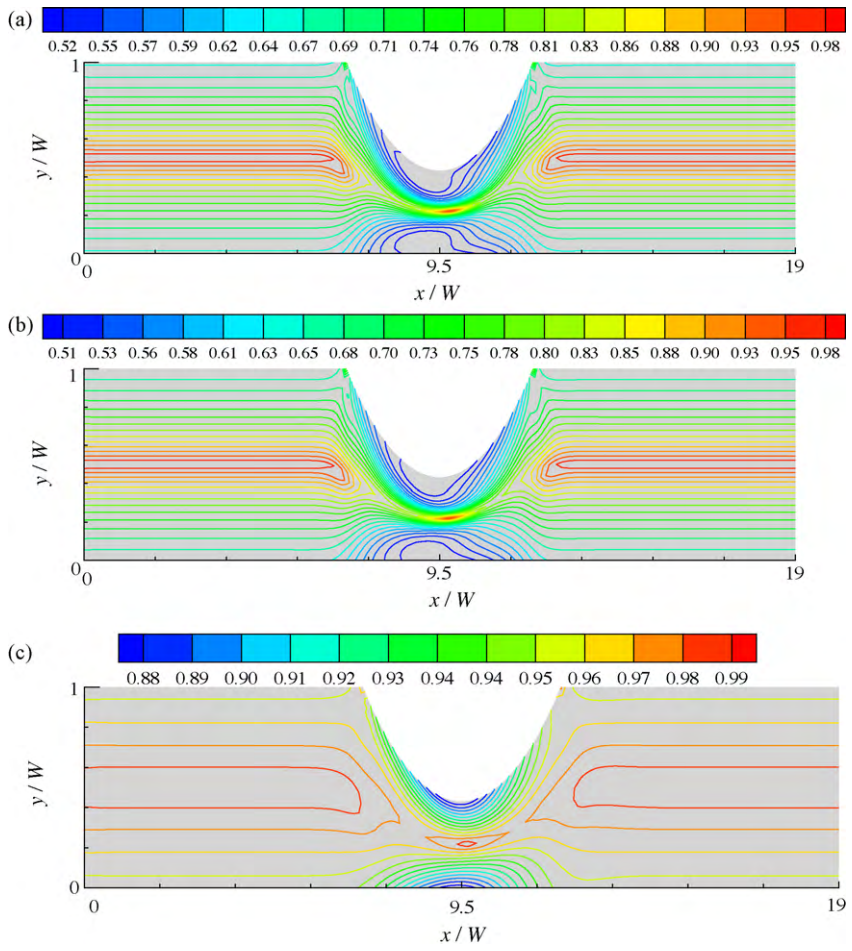

Fig. 5. Contour plots of the smallest eigenvalues (m_1) of the conformation tensor at $Wi = 0.1$ for: (a) Oldroyd-B, (b) FENE-P, and (c) Owens models, at a tension ratio $\alpha = 30$.

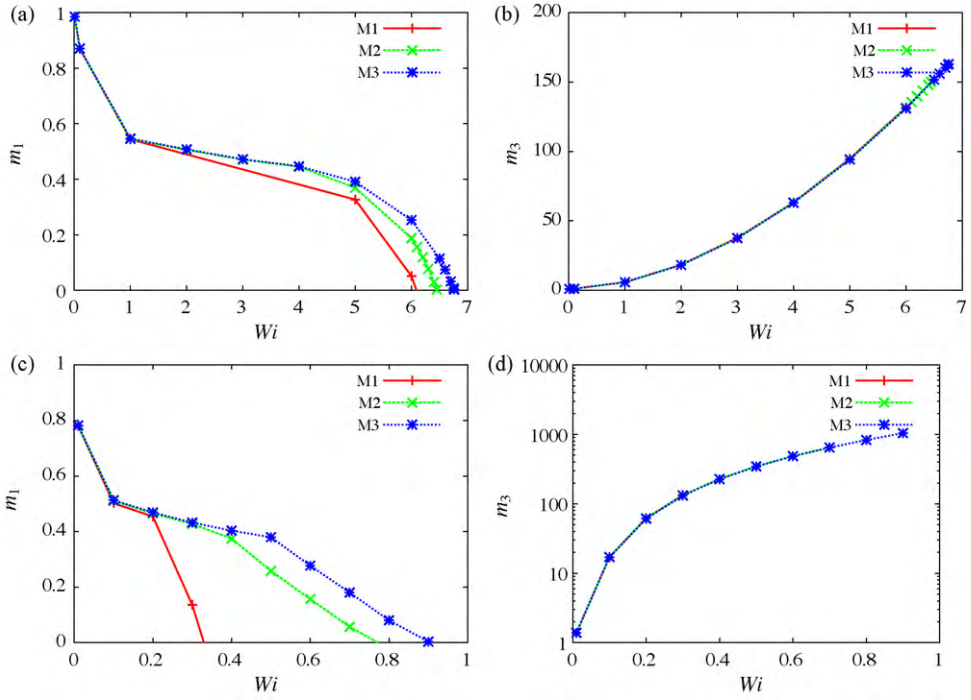

Fig. 6. Maximum value of the largest eigenvalue (m_3) and minimum value of the smallest eigenvalue (m_1) in the entire flow domain, for the Owens model, as a function of Wi at two different values of tension ratio $\alpha = 30$ ((a) and (b)), and $\alpha = 45$ ((c) and (d)).

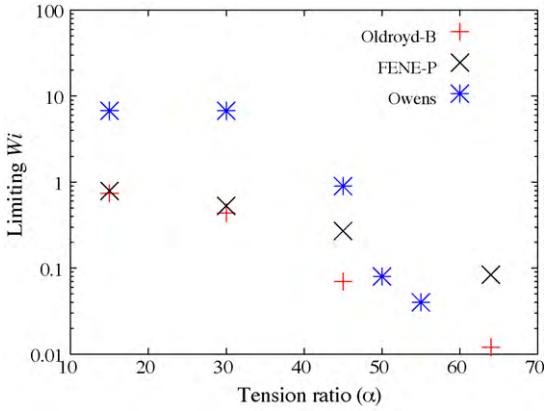

Fig. 7. Limiting Weissenberg number for the Oldroyd-B, FENE-P and Owens models at different tension ratios α.

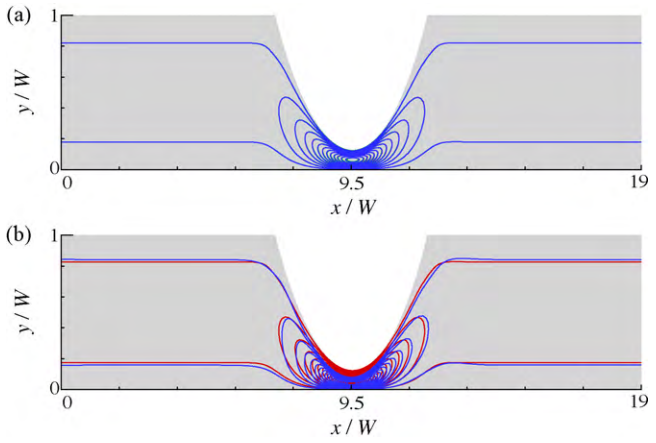

Fig. 9. Contours of axial velocity (v_x) in the flow domain, for (a) Newtonian (red), Oldroyd-B (green) and FENE-P (blue) fluids, and (b) Newtonian (red) and Owens (blue) fluids, at $Wi = 0.01$ and $\alpha = 45$. (For interpretation of the references to colour in this figure legend, the reader is referred to the web version of this article.)

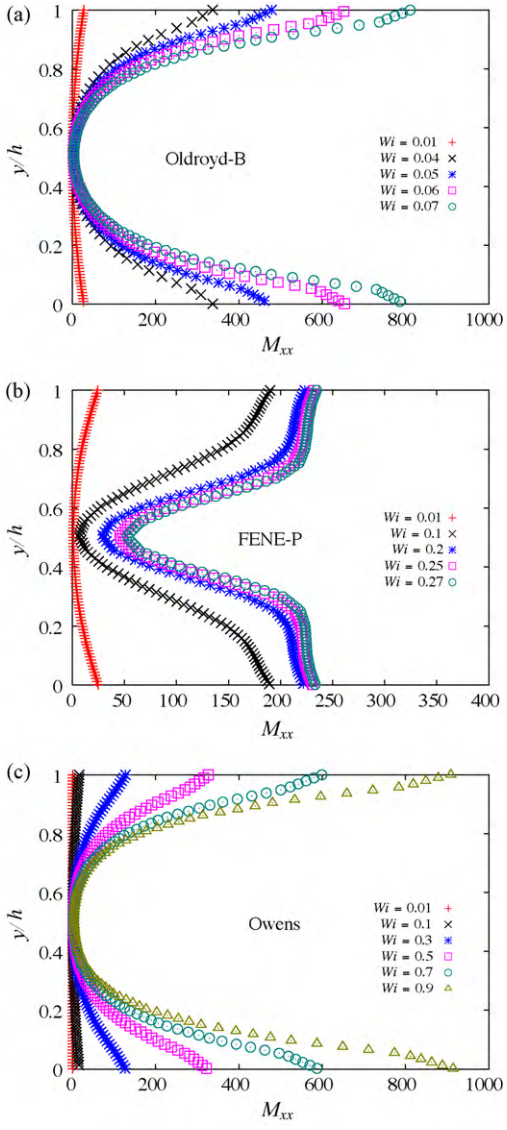

Fig. 8. Profile of M_{xx} across the narrowest channel gap for the Oldroyd-B, FENE-P and Owens models, for a range of Weissenberg numbers, at $\alpha = 45$. The distance from the bottom channel is scaled by the narrowest gap width h of the particular model.

behaviour. These deformation rates are defined as,

$$\dot{\epsilon}_{\mathbf{M}} \equiv \boldsymbol{m}_3\boldsymbol{m}_3 : \mathbf{D} \quad \text{and} \quad \dot{\gamma}_{\mathbf{M}} = |\boldsymbol{m}_1\boldsymbol{m}_3 : \mathbf{D}| \tag{13}$$

where $\dot{\epsilon}_{\mathbf{M}}$ is the mean ensemble molecular extension rate, $\dot{\gamma}_{\mathbf{M}}$ is the mean ensemble molecular shear rate, and, as mentioned earlier, the eigenvectors $\boldsymbol{m}_3$ and $\boldsymbol{m}_1$ are associated with the largest and smallest eigenvalue of $\mathbf{M}$, respectively. In regions of flow where $\dot{\epsilon}_{\mathbf{M}} > 0$, molecular segments are being stretched along their direction of preferred stretch and orientation and the flow is working against the molecular relaxation processes. On the other hand, a large $\dot{\gamma}_{\mathbf{M}}$ indicates that the rate of strain is deforming molecules aligned along one of the principal directions of the conformation tensor, in a direction orthogonal to their orientation.

Figs. 10 and 11 display contours of molecular extension and shear rate for the Oldroyd-B, FENE-P and Owens fluids at $\alpha = 30$ and $Wi = 0.1$. Fig. 10 indicates that $\dot{\epsilon}_{\mathbf{M}}$ is of the same order of magnitude for the Oldroyd-B and FENE-P models, and the contour lines appear similar to each other. However, both the contours and the maximum value for the Owens model are significantly different, with the maximum value being greater by roughly a factor of 3. With regard to $\dot{\gamma}_{\mathbf{M}}$, on the other hand, while the contour lines are similar in all the fluid models, the maximum values for the Oldroyd-B and FENE-P models are roughly greater than that for the Owens model by a factor of 6 (Fig. 11).

A comparison of the contour lines for the largest eigenvalue m_3 (displayed in Fig. 4) with the contour lines for $\dot{\gamma}_{\mathbf{M}}$ (Fig. 11), suggests a strong correlation between the two sets of figures. Indeed, the ordering of the magnitudes between the three models, with the values for the Oldroyd-B and FENE-P models being greater than that for the Owens model, is similar in both figures. A more detailed examination of this correlation is afforded by Fig. 12, which shows the location of the maximum values of m_3, $\dot{\gamma}_{\mathbf{M}}$, $\dot{\epsilon}_{\mathbf{M}}$, and the local Weissenberg number $\widetilde{Wi}$, for the Owens model at $\alpha = 45$, for a range of Wi. For all values of the Weissenberg number, the maximum values of m_3, $\dot{\gamma}_{\mathbf{M}}$ and $\widetilde{Wi}$ coincide with each other, and are located just below the collapsible channel, as suggested by the contour lines in Figs. 4 and 11 for the former two variables. Note that the location appears to move slightly upstream with increasing Wi. On the other hand, the location of the maximum value of $\dot{\epsilon}_{\mathbf{M}}$ starts close to the bottom of the collapsible membrane for small values of Wi, but moves away towards the bulk flow with increasing Wi. It seems that it is the maximum molecular shear rate below the collapsible membrane rather than the maximum molecular extension rate that determines the magnitude of the largest eigenvalue.

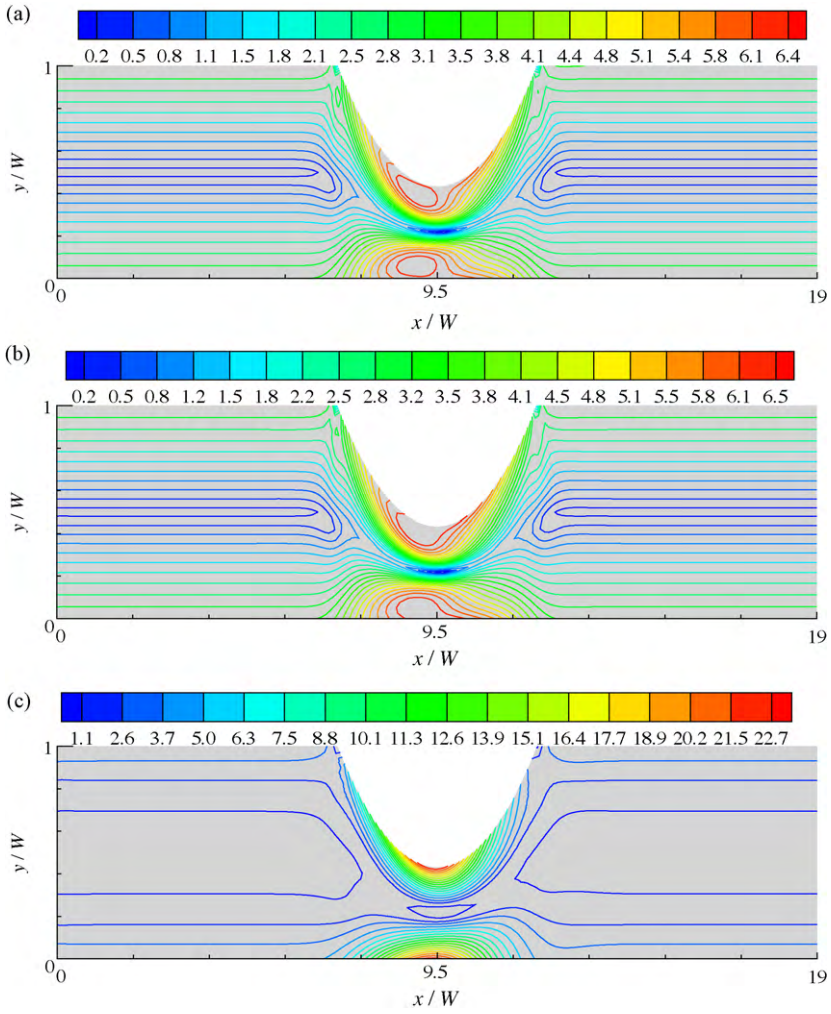

Fig. 10. Molecular extension rate $\dot{\epsilon}_{\mathbf{M}}$ for (a) Oldroyd-B, (b) FENE-P, and (c) Owens models, at $Wi = 0.1$ and $\alpha = 30$.

It is appropriate here to revisit Fig. 6(b) and (d) to note the change in the shape of the m_3 versus Wi curve with an increase in α from 30 to 45. While at $\alpha = 30$ the slope of the curve *increases* with increasing Wi, the slope *decreases* with increasing Wi at $\alpha = 45$. The value of m_3 also appears to be levelling off in the latter case. In their examination of the slot coating flow of a viscoelastic fluid, Bajaj et al. [37] also observed that the maximum m_3 versus Wi curve changes slope and goes through an inflection point with increasing Wi. In that context, it was found that the shape change was related to the fact that the location of the maximum eigenvalue changed from being near a shear-dominated region adjacent to the moving web supporting and transporting the fluid, to being near the extension-dominated region just below the free-surface. In the present instance however, the maximum eigenvalue always appears to be located just below the deformable membrane for all the values of α that we have examined, and coincides with the location of $\dot{\gamma}_{\mathbf{M}}$, as has been demonstrated in Fig. 12.

3.4. Flexible membrane shape, and pressure and stress fields

In the remainder of this work, we focus our attention on examining the influence of the Weissenberg number Wi and the tension ratio α on the shape of the membrane, and on stress and conformation tensor fields in the channel, for the fixed values of the viscosity ratio β, the non-dimensional transmural pressure difference P_d, and Reynolds number Re, that have been adopted here. We start by examining the dependence of the shape of the channel on Wi and α, for each of the three viscoelastic fluids, and subsequently attempt to explain the origin of the observed dependence.

Fig. 13(a) displays the shape of the flexible wall, for the three fluid models, at various values of α, for a fixed value of $Wi = 0.01$, and Fig. 13(b) is a zoomed in view of the membrane shape close to the centre of the membrane, for the three fluids, at various values of Wi, for a fixed value of $\alpha = 45$. It is clear from Fig. 13(a) that on the scale of the figure, the shape of the membrane for the Oldroyd-B and FENE-P models is indistinguishable from the shape of the membrane for a Newtonian fluid at all three values of α (=15, 30 and 45). On the other hand, the shape of the membrane for the Owens model, in the neighbourhood of the centre of the membrane, becomes clearly distinguishable from that for a Newtonian fluid at $\alpha = 45$. For each of the three fluid models, the curve corresponding to $Wi = 0.01$ in Fig. 13(b) is the same as that in Fig. 13(a) for $\alpha = 45$. In the case of the Owens model, since the curves for $Wi = 0.1$ and $Wi = 0.5$ coincide with the curve for $Wi = 0.01$, it is clear that the Weissenberg number has negligible influence on the shape of the membrane. While there appears to be a slight change in the shape of the membrane for the Oldroyd-B fluid, the most significant change occurs for the FENE-P model, with the shape approaching that for the Owens model with increasing Weissenberg number. From the nature of the boundary condition on the flexible membrane adopted here (Eq. (9)), it is clear that the only reason the membrane can change shape as a result of changing either α or Wi is due to a change in the normal stress acting on the membrane. In the present formulation, the shear stress has no

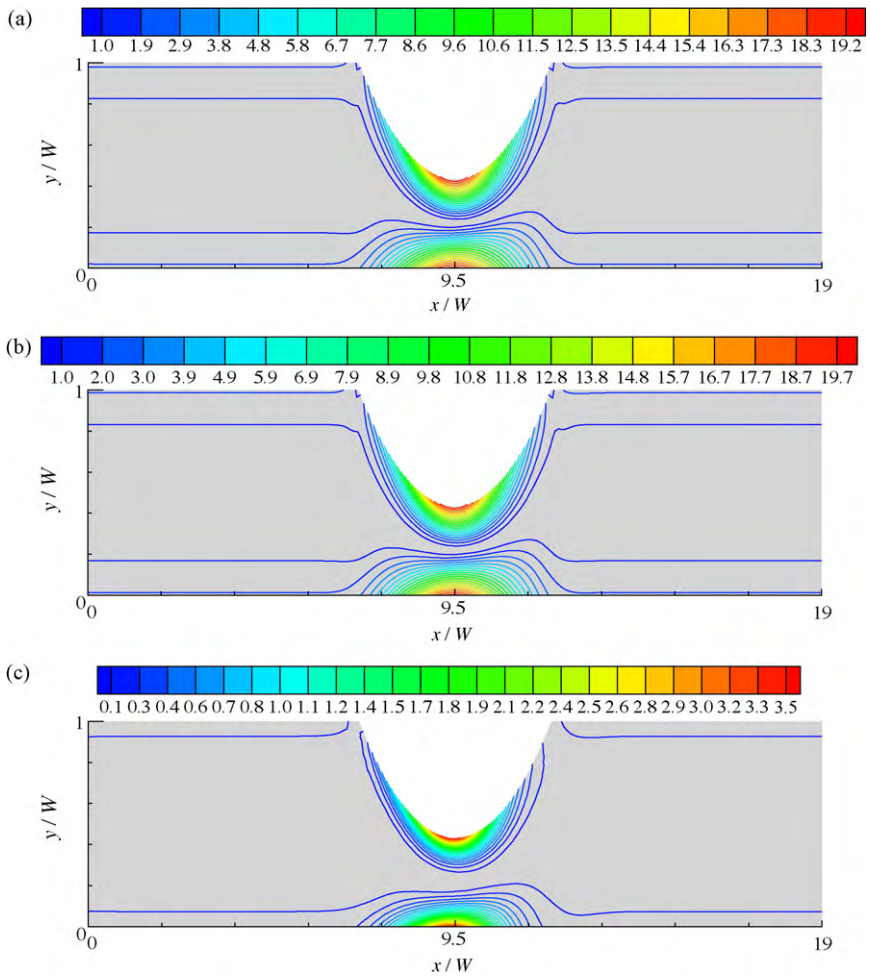

Fig. 11. Molecular shear rate $\dot{\gamma}_{\mathbf{M}}$ for (a) Oldroyd-B, (b) FENE-P, and (c) Owens models, at $Wi = 0.1$ and $\alpha = 30$.

influence on membrane shape. It is reasonable therefore to examine the normal stress field on the flexible membrane in order to find the cause of the change (or lack thereof) in the shape of the membrane for the three fluids.

Fig. 14(a)–(c) shows plots of the total non-dimensional normal stress (T_n), and the individual contributions of the non-dimensional pressure (P), the non-dimensional viscous normal stress (τ_n), and the non-dimensional elastic normal stress (σ_n), for the three viscoelastic fluids, on the flexible membrane as a function of distance along the membrane. The pressure and viscous normal stress for a Newtonian fluid is also displayed on each subfigure for the purpose of comparison. The vertical line indicates the midpoint of the collapsible membrane ($9.5W$), which is the location of the narrowest channel gap for most of the cases. It is immediately apparent that the only contribution to the normal stress is the pressure, since both τ_n and σ_n are identically zero for all the fluids. This result is entirely consistent with the analytical result derived by Patankar et al. [41] that any incompressible fluid with a constitutive model of the following form,

$$a_1\mathbf{D} + a_2\overset{\nabla}{\mathbf{D}} + a_3\mathbf{T} + a_4\overset{\nabla}{\mathbf{T}} = \mathbf{0} \tag{14}$$

will have a zero normal component of extra stress on a rigid body surface. Here, a_1, a_2, a_3, and a_4 are constants or some scalar functions of the invariants of $\mathbf{D}$ and $\mathbf{T}$, and $\overset{\nabla}{\mathbf{D}}$ and $\overset{\nabla}{\mathbf{T}}$ represent the upper convected time derivatives of $\mathbf{D}$ and $\mathbf{T}$. It can be shown that all the viscoelastic fluids considered here belong to the class of fluids described by Eq. (14). Since the shape of the flexible membrane is entirely determined by the normal force acting on it, the consequence of zero normal components of extra stress is that only differences in the predictions of pressure on the membrane between one model and another are responsible for any differences in the prediction of the shape of the membrane. Clearly, at $\alpha = 45$, the pressure exerted by the Oldroyd-B and FENE-P fluids along the membrane is nearly identical to that exerted by a Newtonian fluid, while the pressure exerted by an Owens model fluid is significantly

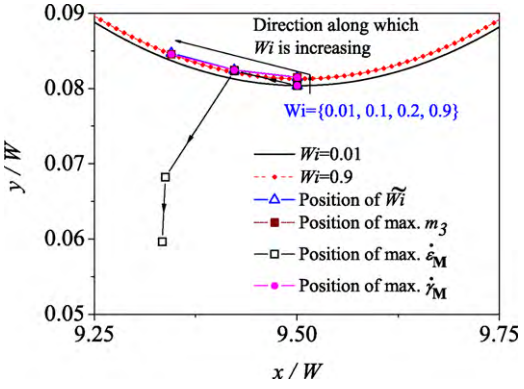

Fig. 12. Locations of the maximum eigenvalue m_3, the maximum molecular shear and extension rates $\dot{\gamma}_{\mathbf{M}}$ and $\dot{\epsilon}_{\mathbf{M}}$, and the maximum local Weissenberg number $\widetilde{Wi}$, for the Owens model, at $\alpha = 45$, for various values of the Weissenberg number Wi. Curved lines indicate the shape of the flexible membrane at the lowest and highest value of Wi.

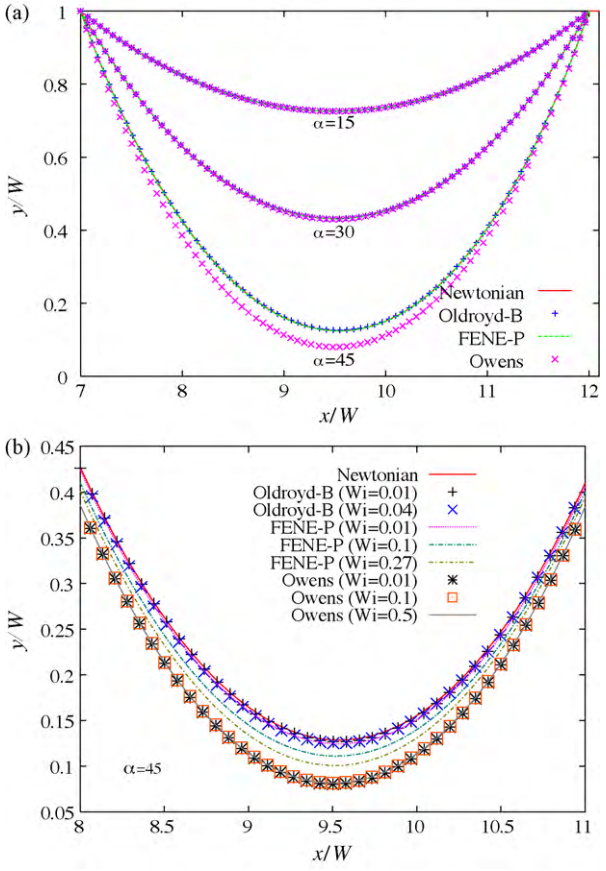

Fig. 13. The deformed shape of the flexible wall for the steady flow of Oldroyd-B, FENE-P and Owens model fluids in a 2D collapsible channel, compared with the profile for a Newtonian fluid, with $Re = 1.0$ and $\beta = 0.0071$, at (a) various values of α for $Wi = 0.01$, and (b) various values of Wi for $\alpha = 45$.

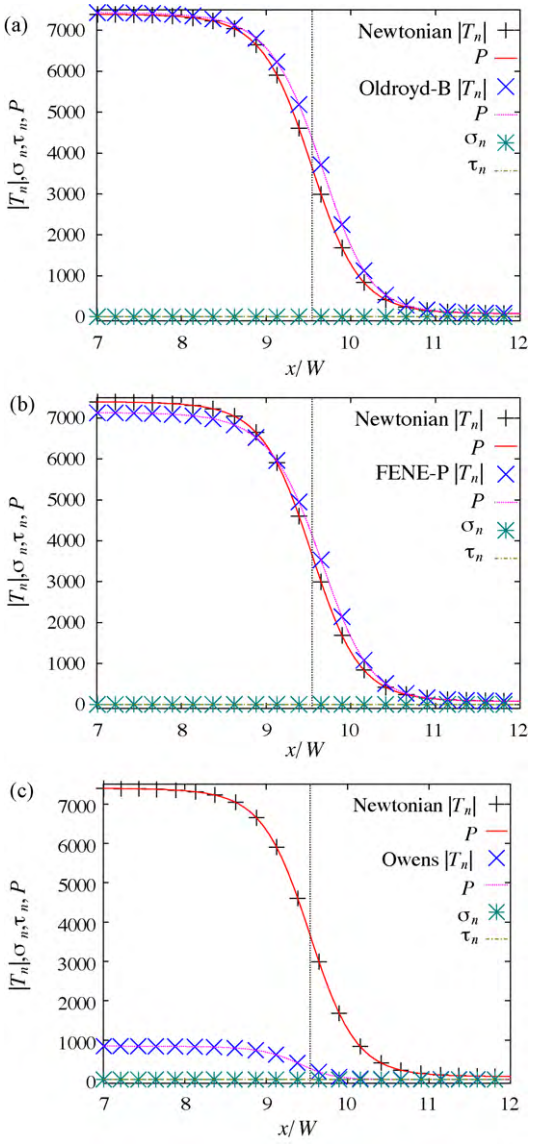

Fig. 14. Pressure and normal components of stress on the flexible wall for the Newtonian, Oldroyd-B, FENE-P and Owens models at $\alpha = 45$ and $Wi = 0.01$, with $Re = 1.0$ and $\beta = 0.0071$. T_n is the normal component of total stress, P is the pressure, τ_n is the normal component of viscous stress and σ_n is the normal component of elastic stress.

lower. This difference is responsible for the difference observed earlier in the predicted membrane shape in Fig. 13(a). The origin of the pressure difference predicted by the different models is examined in greater detail after first discussing the results in Fig. 15.

The two sets of plots in Fig. 15 display the dependence of the pressure profile on Wi and α for all the three viscoelastic fluids. From Fig. 15(a)–(c) it can be seen that an increase in Wi leads to a decrease in the pressure upstream of the narrowest gap in the channel, while causing a modest increase in the pressure downstream of the narrowest gap. In each of the subfigures, data is presented until the limiting Weissenberg number for the respective model. Fig. 15(d)–(f) reveals that the pressure increases uniformly across the entire channel with an increase in α. Both the Oldroyd-B and FENE-P fluids closely mirror the increase in pressure observed for a Newtonian fluid (represented by the symbols). On the other hand, as seen earlier in Fig. 14(c), the pressure prediction in the Owens model is below the Newtonian value at all values of α. The increase in pressure is not surprising since the narrowest channel gap decreases with increasing α (see Fig. 13(b)). Note that results are reported in Fig. 15(f) for the Owens model for a maximum value of $\alpha = 45$. This is discussed further subsequently.

We now examine the possible origin of the differences in the prediction of pressure by the different models. Since the Oldroyd-B and the FENE-P models predictions of pressure are close to that for a Newtonian fluid at $Wi = 0.01$, it can be conjectured that the elasticity of the fluid accounted for by these two models does not play a significant role in determining the pressure. Since the Owens model at the same value of Wi predicts a significantly lower pressure, it seems reasonable to expect that the shear thinning behaviour of the Owens model is the source of this difference. In order to examine this hypothesis further, we have plotted in Fig. 16(a), the FENE-P and Owens models predictions of the microstructure's contribution to viscosity (η_p) as a function of the local Weissenberg number $\widetilde{Wi}$, in a steady shear flow, at a constant value of λ_0. For the values of U_0 and W chosen here, this value of λ_0 corresponds to an inlet Weissenberg number of 0.1. The dependence of η_p on $\dot{\gamma}$ for a FENE-P model in steady shear flow has been derived previously [42].

For the Owens model, the dependence of η_p on $\dot{\gamma}$ in steady shear flow is given by Eq. (7). Since the parameters in the Cross model are fixed for all the computations carried out here, the functional dependence of η_p on $\dot{\gamma}$ is the same in all the cases considered here. However, since the profile in Fig. 16(a) for the Owens model is plotted as a function of the local Weissenberg number $\widetilde{Wi}$, it will vary for different values of λ_0.

For the parameters in the Owens model adopted here (chosen by Owens [23] to get agreement with the experimental results of Bureau et al. [38]), it is clear from Fig. 16(a) that the onset of shear thinning occurs at really small values of $\widetilde{Wi}$. If shear thinning is the

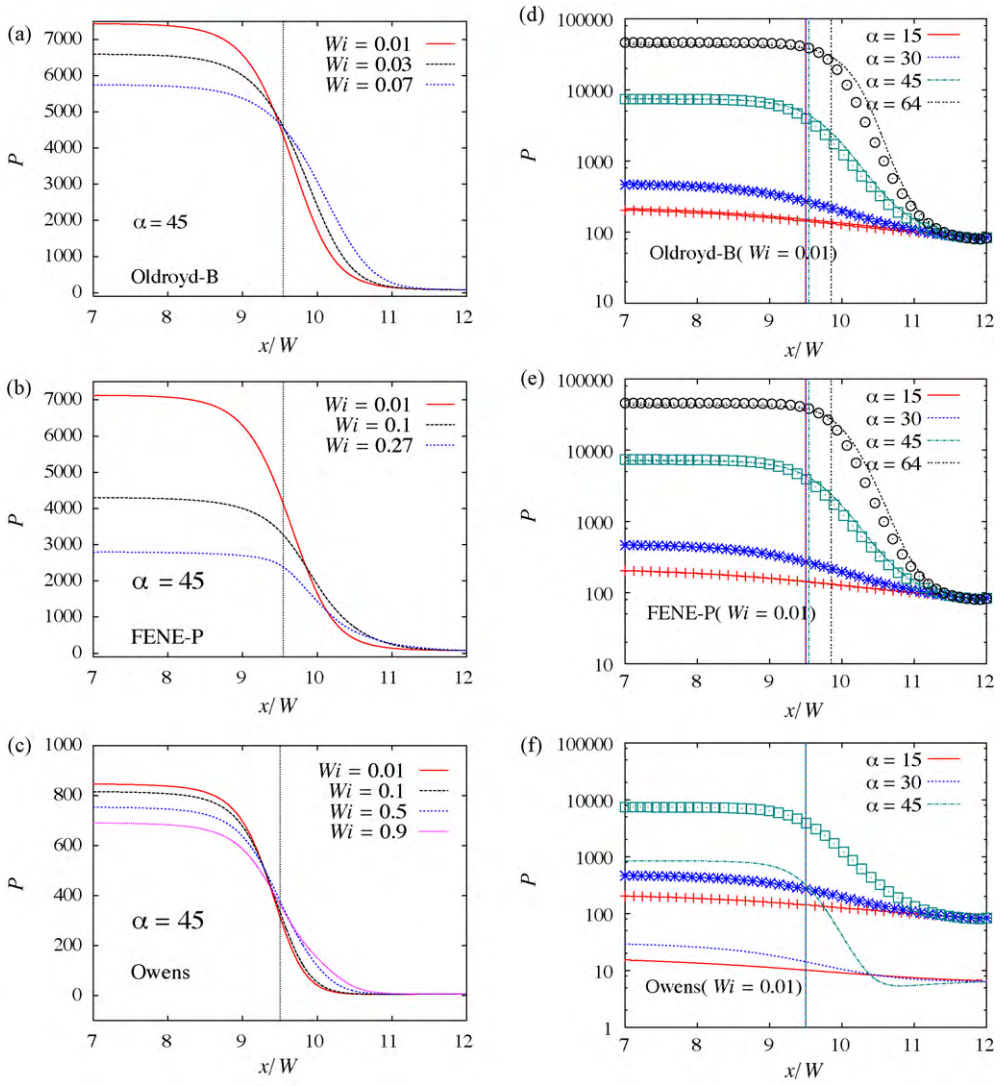

Fig. 15. Dependence of the pressure profile along the flexible membrane on Wi and α, for the Oldroyd-B ((a) and (d)), FENE-P ((b) and (e)) and Owens models ((c) and (f)), respectively. The symbols in (d)–(f) are for a Newtonian fluid. Note that $\alpha = 45$ in (a)–(c) and $Wi = 0.01$ in (d)–(f). All other parameters are as in Fig. 14.

sole cause for the reduced prediction of pressure on the membrane in a channel flow, then a Newtonian fluid with viscosity equal to the effective viscosity in the Owens model, would predict the same value of pressure as the Owens model. By scanning the flow field in the channel, the maximum value of $\widetilde{Wi} = \lambda_0 \dot{\gamma}$ (which occurs just below the collapsible membrane) for an inlet Weissenberg number $Wi = 0.1$ and $\alpha = 45$, was found to be $\widetilde{Wi} = 91.6$. As indicated in Fig. 16(a) for the Owens model, this corresponds to a reduced viscosity of $\eta_p = 0.0043$ at the location of the maximum shear rate. In Fig. 16(b), the pressure profile along the flexible membrane predicted by the Owens model at $Wi = 0.1$ and $\alpha = 45$, has been compared with pressure profiles predicted for Newtonian fluids with a wide range of viscosity values. Of these, the profile for a Newtonian fluid with a viscosity $\eta_0 = \eta_p + \eta_s = 0.0043 + 0.001 = 0.0053$ Pa s is nearly identical to that for the Owens model, strongly supporting the validity of our hypothesis. Fig. 16(a) indicates that even the FENE-P fluid suffers considerable shear thinning at $Wi = 0.1$. By following a procedure similar to that for the Owens model, we find that the maximum value of $\widetilde{Wi}$, at $Wi = 0.1$ and $\alpha = 45$, for a FENE-P fluid flowing in the channel is 44.4. This corresponds to $\eta_p = 0.0513$. As can be seen in Fig. 16(b), the pressure profile on the flexible membrane for a Newtonian fluid with $\eta_0 = 0.0523$ is fairly similar to that for a FENE-P fluid. In particular, the value for the maximum pressure on the membrane is nearly identical.

The identification of shear thinning as the main factor responsible for the predicted pressure profile is also helpful in understanding the dependence of the pressure drop ΔP in the channel, on the inlet Weissenberg number, depicted in Fig. 17(a). (Note that the curves terminate at the limiting Wi for each model). Clearly, the lack of any change in the pressure drop with Wi for an Owens model fluid is related to the fact that at these Weissenberg numbers, nearly all the shear thinning that can occur has occurred, and there is consequently no change in the viscosity with increasing Wi. The fairly rapid decrease in pressure drop for a FENE-P fluid is related to the significant shear thinning that sets in at Weissenberg numbers greater than 0.1 (which correspond to $\widetilde{Wi} \geq 1$). Interestingly, the modest decrease in ΔP with increasing Wi observed for the Oldroyd-B fluid must be attributed to the fluids elasticity, since the Oldroyd-B fluid does not shear thin. Unfortunately, the breakdown of the Oldroyd-B model at very low values of Wi prevents a more thorough examination of the dependence of ΔP on Wi. It is worth noting that the dependence of membrane shape on Wi observed earlier in Fig. 13(b), namely, the lack of change in membrane shape for the Owens model, and the significant change in

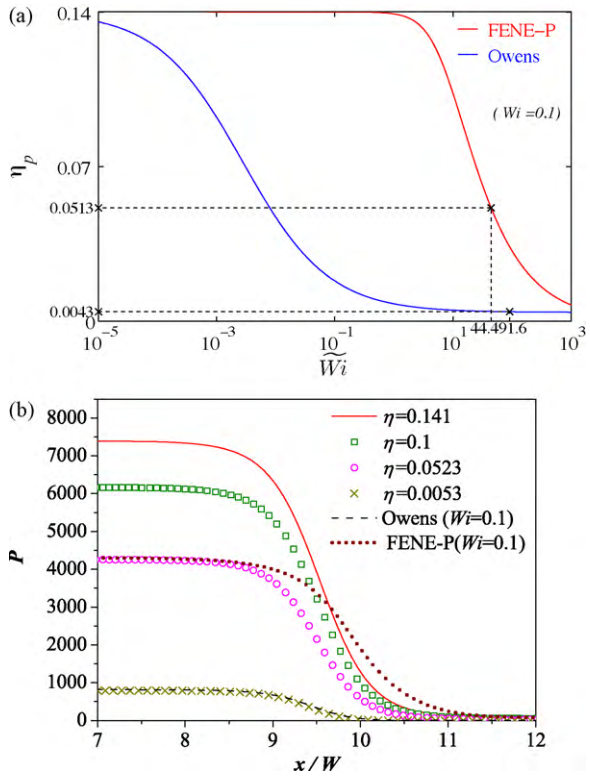

Fig. 16. (a) The contribution of the microstructure to the total viscosity, η_p, for the Owens model and FENE-P fluids in steady shear flow as a function of local Weissenberg number $\widetilde{Wi}$, at a constant value of the relaxation time λ_0. (b) Pressure profile along the flexible membrane for Newtonian fluids with a range of viscosities. The profiles for an Owens model fluid and a FENE-P fluid, with $Wi = 0.1$ and $\alpha = 45$, are also displayed.

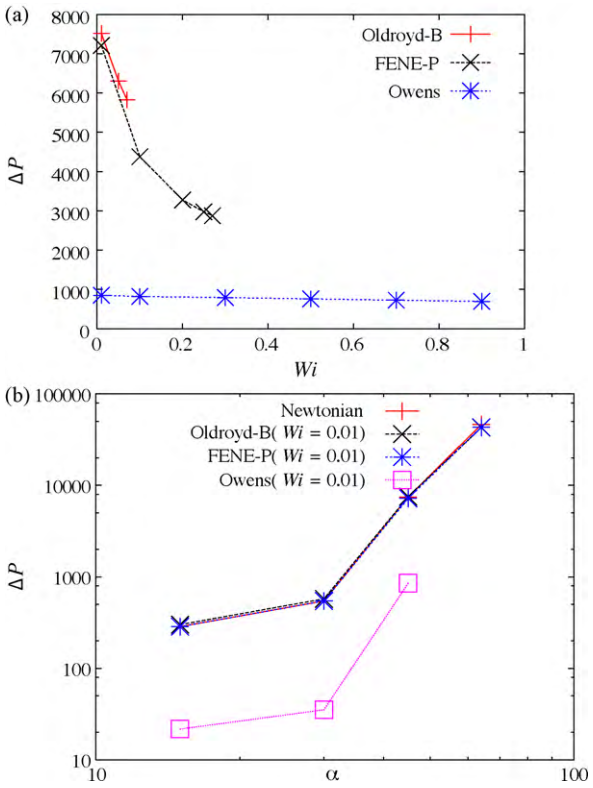

Fig. 17. (a) Pressure drop ΔP in the channel for the Oldroyd-B, FENE-P and Owens models at different Wi, for $\alpha = 45$, $Re = 1.0$ and $\beta = 0.0071$. Note that for a Newtonian fluid, $\Delta P = 7474.0$. The curves terminate at the limiting Weissenberg number for each model. (b) Dependence of pressure drop on tension ratio for the three viscoelastic fluids, at $Wi = 0.01$, compared to the dependence of ΔP on α for a Newtonian fluid.

shape for the FENE-P model, can also be understood in the context of the shear thinning behaviour of these two fluids. The increase in ΔP with α displayed in Fig. 17(b) is clearly the result of the narrowing of the channel gap with increasing α. The coincidence of the curves for the Oldroyd-B and FENE-P fluids with that for a Newtonian fluid is because the viscosities of these fluids are nearly identical at $Wi = 0.01$.

The dependence on α of the narrowest channel gap (scaled by the width of the channel) predicted for the three viscoelastic models, is compared with that for a Newtonian fluid in Fig. 18(a). The rate at which the narrowest gap decreases with increasing α appears to slow down for $\alpha \geq 50$ in the case of Newtonian, Oldroyd-B and FENE-P models. While the behaviour of the Owens model coincides with that of the other fluids until approximately $\alpha = 45$, the gap continues to decrease until it becomes extremely narrow. Indeed, the gap becomes so small for $\alpha \geq 50$ that we have been unable to compute the shape of the membrane for any values of $\alpha > 55$. On the other hand, no difficulty was encountered in computing the membrane shape for the Oldroyd-B and FENE-P models for all the values of α explored here (up to $\alpha = 64$). The difficulty of numerically solving the Owens model for $\alpha \geq 50$ is the likely cause for the change in the dependence of the liming Weissenberg number on α, observed earlier at these values of α in Fig. 7. In Fig. 18(b), the dependence on Wi of the narrowest channel gap scaled by the value of the gap for a Newtonian fluid, $h/h_{\text{Newtonian}}$, is displayed. The differences observed between the three viscoelastic fluids can be understood in terms of the differences in the degree of shear thinning exhibited by these fluids, using arguments similar to those proposed above in the context of Fig. 17(a).

Fig. 19(a)–(c) displays the dependence of the axial component of the conformation tensor M_{xx} along the flexible membrane on Wi, and Fig. 19(d)–(f) displays its dependence on α. As expected, an increase in Wi or in α leads to an increase in the degree of stretching experienced by the microstructural elements, with the maximum stretching occurring near the narrowest channel gap (indicated by the vertical lines). Since both the Oldroyd-B and Owens constitutive equations are based on Hookean dumbbell models, there is no upper bound on M_{xx}. Interestingly, the FENE-P model predicts that close to the limiting Weissenberg number, the microstructural elements are nearly fully stretched for a fairly significant fraction of the length of the flexible membrane. For large values of α, the shape of the curves in Fig. 19(d) and (e) appears to reflect the asymmetry in the shape of the membrane, which was seen to occur earlier for Newtonian fluids in Fig. 2. Interestingly, Fig. 19(f) suggests that the value of M_{xx} in the Owens model is much less sensitive to the value of α compared to the Oldroyd-B and FENE-P fluids, and remains nearly unchanged from its equilibrium value. This can be attributed to the extensive shear thinning experienced by the fluid, leading to a significant reduction in the local relaxation time. The same argument can also be used to understand the differences in the relative magnitudes of the maximum eigenvalue m_3 for the three viscoelastic fluids, which is displayed earlier in Fig. 4.

The manner in which the presence of a flexible wall has been treated in this work, through a zero-thickness membrane that is coupled to the fluid only through the normal force, is a particularly simple representation of the fluid–structure interaction problem that underlies flow in a collapsible channel. It is reasonable to expect that the shear force on the membrane will also play a significant role in determining the shape of the membrane. With a view to examining the magnitude of shear forces on the membrane, we have computed the tangential shear stress along the length of

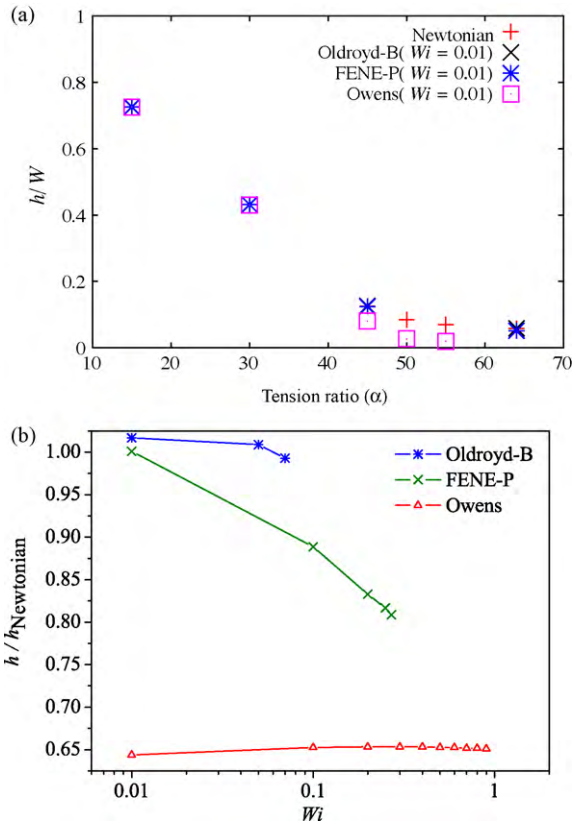

Fig. 18. Dependence of the narrowest channel gap h on: (a) α and (b) Wi. The narrowest gap is scaled by the channel width W in (a), and by the gap for a Newtonian fluid in (b).

the membrane surface. The dependence of the shear stress on both Wi and α, for the three different viscoelastic fluids, is displayed in Fig. 20(a)–(f). It is immediately apparent from Fig. 20(a)–(c) that, while the common feature between the three fluids is the decrease in tangential shear stress with an increase in Wi, there are striking differences in the extent of the decrease. While the Oldroyd-B model fluid suffers a relatively modest decrease in the shear stress near the narrowest channel gap, the FENE-P model fluid experiences a significant decrease. In the case of the Owens model, there is hardly any difference in the shear stress for the different Weissenberg numbers. As has been argued in a number of instances above, it is straightforward to relate these differences in behaviour to the different degrees of shear thinning experienced by the fluids, at the Weissenberg numbers examined in Fig. 20(a)–(c). For all the fluids, at $Wi = 0.01$, the tangential shear stress appears to increase with an increase in α, as can be seen from Fig. 20(d)–(f). While the values for the Oldroyd-B and FENE-P models are approximately equal to each other, the shear stress prediction by the Owens model is significantly lower. At this value of Wi, the FENE-P model fluid does not undergo much shear thinning, and as a result, both the pressure (see Fig. 15(d)–(f)) and the shear stress are similar for the Oldroyd-B and FENE-P models.

In general, even though there are significant differences in the shear stresses predicted by the different models, this is not reflected in the predicted shape of the membrane (see Fig. 13) because of the boundary condition adopted here. It would be extremely interesting to compare the predictions of the three fluid models with more realistic boundary conditions, where the influence of the shear stress is taken into account, since we can anticipate that significant differences in the predicted shape of the membrane will emerge.

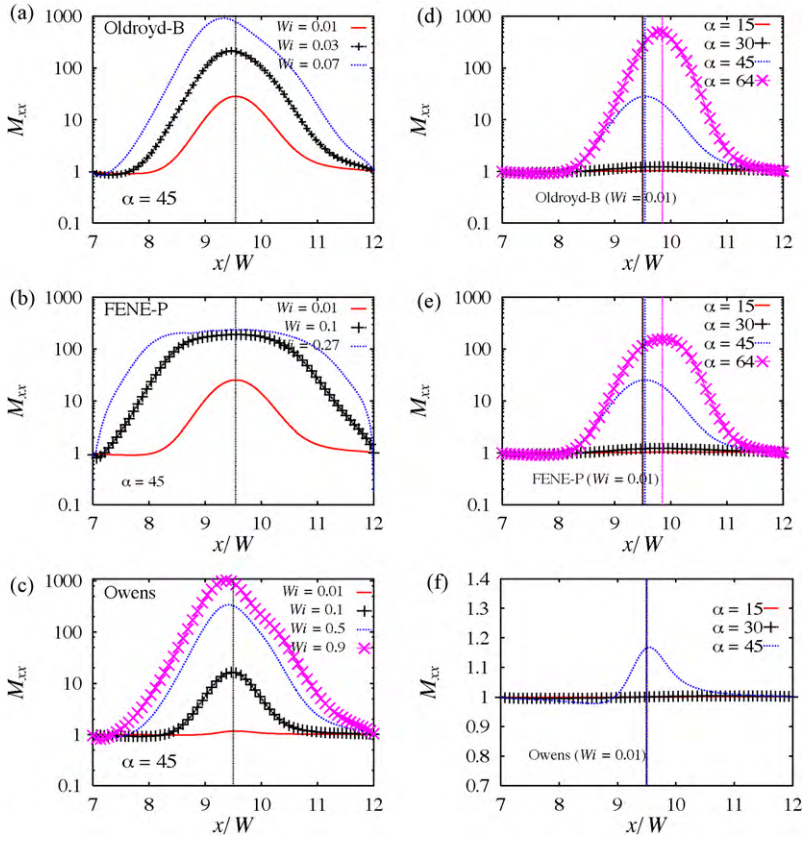

Fig. 19. Dependence of the axial component of the conformation tensor M_{xx} on Wi, for (a) Oldroyd-B, (b) FENE-P, and (c) Owens models, at $\alpha = 45$, and dependence of M_{xx} on α, for (d) Oldroyd-B, (e) FENE-P, and (f) Owens models, at $Wi = 0.01$.

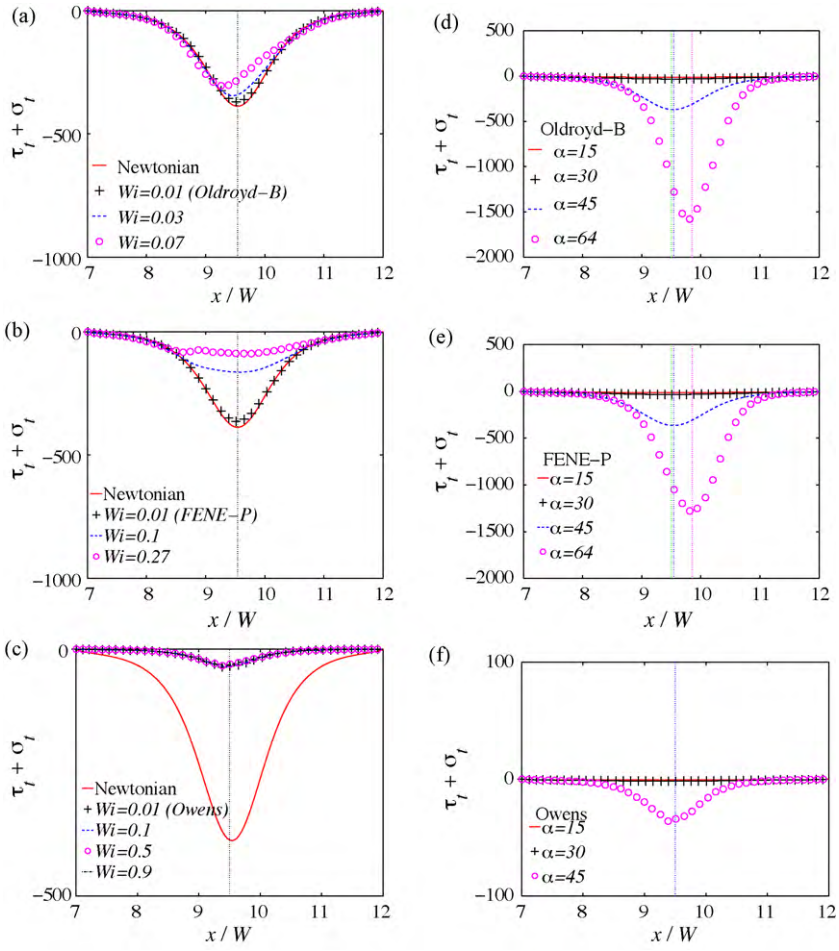

Fig. 20. Dependence of the total tangential shear stress on the membrane ($\tau_t + \sigma_t$) on *Wi*, for (a) Oldroyd-B, (b) FENE-P, and (c) Owens models, at $\alpha = 45$, and dependence of ($\tau_t + \sigma_t$) on α, for (d) Oldroyd-B, (e) FENE-P, and (f) Owens models, at $Wi = 0.01$.

4. Conclusions

The flow of viscoelastic fluids in a two-dimensional channel, in which part of the top wall has been replaced by a membrane under tension, has been studied numerically with the help of the DEVSS-TG/SUPG mixed finite element method. Since the focus has been on modelling flows at low Reynolds number, a fixed value of $Re = 1$ has been used in all the computations. So far, the 2D collapsible channel problem has been studied extensively only for Newtonian fluids. The aim here has been to examine the differences that arise when three different viscoelastic fluids interact with the deformable membrane on the channel wall. Each of the three model viscoelastic fluids that have been chosen, namely, the Oldroyd-B, the FENE-P and Owens models, has unique features that distinguish it from the others. These differences lead to differences in the predictions of the various properties, and in many instances, the source of the difference can be traced back to a particular characteristic of the viscoelastic fluid.

The most significant conclusions of this work are the following:

1. There is a limiting Weissenberg number *Wi* for each of the fluids beyond which computations fail. The value of *Wi* at which simulations breakdown coincides with the value at which the smallest eigenvalue of the conformation tensor becomes negative somewhere in the flow field (see Fig. 6).
2. For the Oldroyd-B and Owens models, the breakdown of numerical computations is accompanied by the axial component of the conformation tensor M_{xx} assuming large values at the top and bottom walls, close to the location in the channel where the gap between the walls is the narrowest (see Fig. 8).
3. The maximum deformation of the microstructural elements occurs at a point just below the deformable membrane at the narrowest gap in the channel, and the location of this point coincides with the location of the maximum shear rate (see Fig. 12).
4. The shape of the deformable membrane, and its dependence on *Wi* and tension ratio α, is entirely determined by the pressure on the membrane surface, and by the changes in pressure that occur as a result of changes in these parameter values (see Figs. 13–15, and 18).
5. The key determinant of the pressure in the channel is the effective viscosity of the viscoelastic fluid at the location of the maximum shear rate. This result has been established by showing that a Newtonian fluid with viscosity equal to the effective viscosity has nearly the same pressure profile as the viscoelastic fluid (see Fig. 16).
6. While it has been difficult to discern any noticeable influence of the elasticity of the fluid on the various properties (except perhaps on M_{xx} as seen in Fig. 19(a)–(c)), the degree of shear thinning exhibited by the fluid has a dramatic effect on all the properties. Thus, for instance, the observed dependence on *Wi* and α, of the pressure drop in the channel (Fig. 17), the width of the narrowest gap (Fig. 18), and the tangential shear stress on the membrane surface (Fig. 20), can be understood by considering the extent of shear thinning experienced by the fluids at the relevant values of these parameters.

7. The significant differences that arise amongst the three viscoelastic fluids in the predicted value of the tangential shear stress on the membrane surface (see Fig. 20), has no influence on the shape of the deformable membrane in the present model because of the boundary condition adopted in this work, whereby only changes in the normal stress on the membrane can lead to changes in the shape. A more accurate model for the deformable membrane would account for the effect of the shear stress on membrane shape. Work is currently underway in our group to develop an algorithm for describing the fluid–structure interaction between a finite deformation elastic solid and a viscoelastic fluid flowing in a collapsible channel.

Acknowledgements

This work was supported by the Australian Research Council under the Discovery Projects program and by the National Science Foundation of the USA under grant DMS-0811160. Computational resources were provided by the Victorian Partnership for Advanced Computation (VPAC), the Monash Sun Grid Cluster, and the Rice University Shared Compute Clusters funded by NSF grants EIA-0216467, CNS-0421109, CNS-0821727, Sun, Sigma Solutions, AMD, and Cray.

References

[1] A.M. Robertson, A. Sequeira, M.V. Kameneva, Hemorheology, in: G.P. Galdi, R. Rannacher, A.M. Robertson, S. Turek (Eds.), Hemodynamical Flows: Modeling, Analysis and Simulation (Oberwolfach Seminars), Birkhauser, 2008, pp. 63–120.
[2] O.K. Baskurt, H.J. Meiselman, Blood rheology and hemodynamics, Semin. Thromb. Hemost. 29 (2003) 435–450.
[3] A.S. Popel, P.C. Johnson, Microcirculation and hemorheology, Ann. Rev. Fluid Mech. 37 (2005) 43–69.
[4] C.D. Bertram, Unstable equilibrium behaviour in collapsible tubes, J. Biomech. 19 (1986) 61–69.
[5] C.D. Bertram, C.J. Raymond, T.J. Pedley, Mapping of instabilities during flow through collapsed tubes of differing length, J. Fluids. Struct. 4 (1990) 125–153.
[6] M.P. Rast, Simultaneous solution of the Navier–Stokes and elastic membrane equations by a finite-element method, Int. J. Numer. Methods Fluids 19 (1994) 1115–1135.
[7] T.W. Lowe, T.J. Pedley, Computation of Stokes flow in a channel with a collapsible segment, J. Fluids Struct. 9 (1995) 885–905.
[8] X.Y. Luo, T.J. Pedley, A numerical simulation of steady flow in a 2-D collapsible channel, J. Fluids Struct. 9 (1995) 149–174.
[9] X.Y. Luo, T.J. Pedley, A numerical simulation of unsteady flow in a 2-D collapsible channel, J. Fluid Mech. 314 (1996) 191–225.
[10] M. Heil, O.E. Jensen, Flows in deformable tubes and channels—theoretical models and biological applications, in: P.W. Carpenter, T.J. Pedley (Eds.), Flow Past Highly Compliant Boundaries and in Collapsible Tubes, Kluwer, Dordrecht, 2003, pp. 15–50.
[11] O.E. Jensen, M. Heil, High-frequency self-excited oscillations in a collapsible-channel flow, J. Fluid Mech. 481 (2003) 235–268.
[12] X. Xie, M. Pasquali, Computing 3D free surface viscoelastic flows, in: A. Mammoli, C.A. Brebbia (Eds.), Moving Boundaries VII: Computational Modelling of Free and Moving Boundary Problems, WIT Press, Southampton, UK, 2003, pp. 225–234.
[13] X. Xie, Modeling viscoelastic free surface and interfacial flows, with applications to the deformation of droplets and blood cells, Ph.D. thesis, Rice University, Houston, TX, 2006.
[14] H.F. Liu, X.Y. Luo, Z.X. Cai, T.J. Pedley, Sensitivity of unsteady collapsible channel flows to modelling assumptions, Commun. Numer. Methods Eng. 25 (2009) 483–504.
[15] A.L. Hazel, M. Heil, Steady finite-Reynolds-number flows in three-dimensional collapsible tubes, J. Fluid Mech. 486 (2003) 79–103.
[16] A. Marzo, X. Luo, C. Bertram, Three-dimensional collapse and steady flow in thick-walled flexible tubes, J. Fluids Struct. 20 (2005) 817–835.
[17] M.C. Williams, J.S. Rosenblatt, D.S. Soane, Theory of blood rheology based on a statistical mechanics treatment of rouleaux, and comparisons with data, Int. J. Polym. Mater. 21 (1993) 57–63.
[18] D. Quemada, A non-linear Maxwell model of biofluids: application to normal human blood, Biorheology 30 (1993) 253–265.
[19] K.K. Yeleswarapu, M.V. Kameneva, K.R. Rajagopal, J.F. Antaki, The flow of blood in tubes: theory and experiment, Mech. Res. Commun. 25 (3) (1998) 257–262.
[20] D. Quemada, Rheological modelling of complex fluids. IV. Thixotropic and thixoelastic behaviour. Start-up and stress relaxation, creep tests and hysteresis cycles, Eur. Phys. J. Appl. Phys. 5 (1999) 191–207.
[21] N. Sun, D.D. Kee, Simple shear, hysteresis and yield stress in biofluids, Can. J. Chem. Eng. 79 (2001) 36–41.
[22] M. Anand, K. Rajagopal, K.R. Rajagopal, A model incorporating some of the mechanical and biochemical factors underlying clot formation and dissolution in flowing blood, Comput. Math. Methods Med. 5 (2003) 183–218.
[23] R.G. Owens, A new microstructure-based constitutive model for human blood, J. Non-Newton. Fluid Mech. 140 (2006) 57–70.
[24] M.A. Moyers-Gonzalez, R.G. Owens, J. Fang, A non-homogeneous constitutive model for human blood. Part 1. Model derivation and steady flow, J. Fluid Mech. 617 (2008) 327–354.
[25] J. Fang, R.G. Owens, Numerical simulations of pulsatile blood flow using a new constitutive model, Biorheology 43 (2006) 637–660.
[26] M.A. Moyers-Gonzalez, R.G. Owens, J. Fang, A non-homogeneous constitutive model for human blood. Part III. Oscillatory flow, J. Non-Newton. Fluid Mech. 155 (2008) 161–173.
[27] R. Fåhraeus, The suspension stability of blood, Physiol. Rev. 9 (1929) 241–274.
[28] R. Fåhraeus, T. Lindqvist, The viscosity of blood in narrow capillary tubes, Am. J. Physiol. 96 (1931) 562–568.
[29] M. Pasquali, L.E. Scriven, Free surface flows of polymer solutions with models based on the conformation tensor, J. Non-Newton. Fluid Mech. 108 (2002) 363–409.
[30] M. Pasquali, L.E. Scriven, Theoretical modelling of microstructured liquids: a simple thermodynamic approach, J. Non-Newton. Fluid Mech. 120 (2004) 101–135.
[31] K.N. Christodoulou, L.E. Scriven, Discretization of free surface flows and other moving boundary problems, J. Comput. Phys. 99 (1992) 39–55.
[32] J.M. deSantos, Two-phase cocurrent downflow through constricted passages, Ph.D. thesis, University of Minnesota, Minneapolis, MN, 1991 (available from UMI, Ann Arbor, MI, order number 9119386).
[33] D.F. Benjamin, Roll coating flows and multiple roll systems, Ph.D. thesis, University of Minnesota, Minneapolis, MN, 1994 (available from UMI, Ann Arbor, MI, order number 9512679).
[34] X. Xie, M. Pasquali, A new, convenient way of imposing open-flow boundary conditions in two- and three-dimensional viscoelastic flows, J. Non-Newton. Fluid Mech. 122 (2004) 159–176.
[35] R. Guénette, M. Fortin, A new mixed finite element method for computing viscoelastic flows, J. Non-Newton. Fluid Mech. 60 (1995) 27–52.
[36] G.A. Zevallos, M.S. Carvalho, M. Pasquali, Forward roll coating flows of viscoelastic liquids, J. Non-Newton. Fluid Mech. 130 (2005) 96–109.
[37] M. Bajaj, J.R. Prakash, M. Pasquali, A computational study of the effect of viscoelasticity on slot coating flow of dilute polymer solutions, J. Non-Newton. Fluid Mech. 149 (2008) 104–123.
[38] M. Bureau, J. Healy, D. Bourgoin, M. Joly, Rheological hysteresis of blood at low shear rate, Biorheology 17 (1980) 191–203.
[39] J.V.D. Zanden, M. Hulsen, Mathematical and physical requirements for successful computations with viscoelastic fluid models, J. Non-Newton. Fluid Mech. 29 (1988) 93–117.
[40] P. Singh, L. Leal, Finite-element simulation of the start-up problem for a viscoelastic fluid in an eccentric rotating cylinder geometry using a third-order upwind scheme, Theor. Comput. Fluid Dyn. 5 (1993) 107–137.
[41] N.A. Patankar, P.Y. Huang, D.D. Joseph, H.H. Hu, Normal stresses on the surface of a rigid body in an Oldroyd-B fluid, ASME J. Fluids Eng. 124 (2002) 279–290.
[42] R.B. Bird, C.F. Curtiss, R.C. Armstrong, O. Hassager, Dynamics of Polymeric Liquids—Volume 2: Kinetic Theory, 2nd edn, John Wiley, New York, 1987.